ADVANCED MATERIALS TECHNOLOGIES
www.advmattechnol.de

Transient Neurovascular Interface for Minimally Invasive Neural Recording and Stimulation

*Adele Fanelli, Laura Ferlauto, Elodie Geneviève Zollinger, Olivier Brina, Philippe Reymond, Paolo Machi, and Diego Ghezzi**

Neural interfaces are used to mitigate the burden of traumatic injuries, neurodegenerative diseases, and mental disorders. However, the transient or permanent placement of an interface in close contact with the neural tissue requires invasive surgery, potentially entailing both short- and long-term complications. To tackle this problem, a transient neurovascular interface for neural recording and stimulation is developed. This endovascular array has been fabricated with facile molding techniques using solely polymeric materials. In vitro experiments have shown promising electrochemical performance for both recording and stimulation, together with a lack of cytotoxicity in cultured cells. The device is compatible with standard endovascular catheters and, once deployed, provide good apposition to a cylindrical structure mimicking a blood vessel. The advantage of this device is twofold. On the one hand, the exploitation of the cerebrovascular system as an access route to the neural tissue avoids invasive surgeries. On the other hand, a transient device may reduce the inflammatory reaction and avoid additional surgeries for removal or replacement. This neurovascular interface combines the benefits of both transient bioelectronics and stent technology in a single device to broaden the range of applications of neural interfaces from neurological diseases and mental disorders to bioelectronics medicine.

1. Introduction

Neurotechnology for neural recording and stimulation opened the door to a deeper understanding of the brain and, at the same time, led to the development of treatments for heavily impairing conditions following traumatic injuries, neurodegenerative diseases, or mental disorders.[1] Although the potential impact of neurotechnology is enormous, its clinical use nowadays is still limited. Many devices require invasive surgery, with related high risks that not always overcome the benefits for the patients. A big step in this direction has been the development of neurovascular interfaces which interact with the neural tissue from within blood vessels. Endovascular procedures are considerably less invasive, are routinely performed and allow for short recovery time.[2] Moreover, neurovascular interfaces do not require craniotomies, reducing the risks associated with the surgical procedure (e.g., susceptibility to seizures). These advantages could increase the chance of patients accepting the treatment.

Neurovascular interfaces developed so far are wires or catheters used as electrodes. Even though these solutions opened the doors to endovascular neural recording and stimulation, their main limitations were the short-term application and the low spatial resolution. The introduction of stent-electrode arrays (e.g., Stentrode) overcame these issues,[2] and the advantages of this technology have been recently demonstrated in preclinical and clinical trials for brain-computer-interface.[3–6] Also, seventeen potential medical targets have been identified where intravascular neuromodulation could replace invasive deep brain stimulation protocols.[7] By accessing the internal cerebral vein or the anterior communicating artery, it would be possible to perform minimally invasive neuromodulation for a wide range of neurological disorders such as Parkinson's, Alzheimer's, essential tremor, depression, and obsessive-compulsive disorders.[7] Furthermore, neurovascular interfaces could be as well applied to the peripheral system for pain relief, motor deficits, bladder control, and stimulation of muscles, among others. However, the main drawback of stent-electrode arrays is the metallic scaffold. A conductive substrate for electrodes makes insulation critical and shortcuts frequent.[3] Also, metallic stents could induce a strong inflammatory response, that could reduce the performances of a neural interface.[8–11] For conventional stent technology, this limitation already led to the development of bioresorbable devices, allowing for a better interaction with the tissue and placement in mechanically solicited areas.[12]

A. Fanelli, Dr. L. Ferlauto, E. G. Zollinger, Prof. D. Ghezzi
Medtronic Chair in Neuroengineering
Center for Neuroprosthetics and Institute of Bioengineering
School of Engineering
École polytechnique fédérale de Lausanne
Chemin des Mines 9, Geneva 1202, Switzerland
E-mail: diego.ghezzi@epfl.ch
Dr. O. Brina, Dr. P. Reymond, Dr. P. Machi
Division of of Neuroradiology
Geneva University Hospital
Rue Gabrielle-Perret-Gentil 4, Geneva 1205, Switzerland

The ORCID identification number(s) for the author(s) of this article can be found under https://doi.org/10.1002/admt.202100176.

DOI: 10.1002/admt.202100176

These limitations motivated us to develop a transient stent-electrode array based on polymeric materials and built via microfabrication techniques. Reducing the inflammatory response by using a thin and soft scaffold will better preserve the neural interface, providing extended durability and better signal quality.[9,13–16] Moreover, whereas in the case of device failure it would not be easy to replace a metallic stent-electrode array, if not impossible at all, a transient device will leave the possibility for replacement, even if complications occur in the mid- or long-term period. Transient bioelectronics already introduced degradable materials in neurotechnology.[17] Unfortunately, these devices have a short durability, from days to a few weeks, due to the fast degradation rate of the dissolvable metals used for the conductive elements. This limited lifetime prevents their use for mid- and long-term applications.[18,19] Our strategy to overcome this problem is a fully polymeric neural interface, using a slowly biodegradable polymer as a scaffold and a conductive polymer as the active component.

In summary, in this work, we introduce a fully polymeric transient neurovascular interface combining the advantages of transient bioelectronics and stent technology in a single device.

2. Results and Discussion

2.1. Manufacturing of the Device

The transient neurovascular interface is a stent-inspired device, whose scaffold consists of poly-ε-caprolactone (PCL): a synthetic polyester approved by the US Food and Drug Administration for several medical applications, such as drug delivery systems, tissue engineering and medical devices.[20] PCL has a long degradation time, from several months to a few years, allowing it to be an insulating and stable scaffold for mid- and long-term applications.[20] Conductive elements are made out of poly(3,4-ethylenedioxythiophene):polystyrene sulfonate (PEDOT:PSS), a conductive biocompatible polymer commonly used in organic photovoltaic cells, and often used as a coating for metallic electrodes in neural interfaces.[21–23] A feature of this device is the absence of metals in electrodes and feedlines, making the device fully polymeric in all components. PEDOT:PSS is here doped with ethylene glycol (EG) for better conductivity, and (3-glycidyloxypropyl)trimethoxysilane (GOPS) for better endurance in aqueous environment.[23,24]

Fabrication of the device using replica molding proved to be facile. Two molds have been manufactured in SU8 (35-µm thick): one with the engraved pattern of the feedlines (mold for encapsulation in **Figure 1**a) and the other with the protruding pattern of the electrodes, feedlines, and pads (mold for substrate in Figure 1a). After covering the two molds with a PSS release layer (Figure 1a, step 1), the PCL solution has been spin-coated on both (Figure 1a, step 2). After releasing the substrate layer, the PEDOT:PSS-based solution has been dispensed along the engraved pattern for electrodes, feedlines, and pads (Figure 1a, step 3). For each electrode unit (electrode, feedline, and pad), ≈2 µL of solution would completely fill the pattern. This amount would correspond to a film thickness of ≈1–2 µm, decreasing from the channel wall to the center (Figure 1b). After cross-linking of the conductive polymer, thin stainless-steel wires (114-µm diameter) have been attached to the pads using a conductive paste (Figure 1a, step 4). The openings for the electrodes have been laser cut in the encapsulation layer (Figure 1a, step 3) and the film has been released (Figure 1a, step 4). After alignment of the two layers (Figure 1a, step 5), heating at 60 °C allowed their quick fusion and fixed the wires contacts in between (Figure 1a, step 6). Finally, the device outline and its characteristic diamond-like holes have been laser cut to allow for easier bending, reduce the amount of material implanted and maintain open sites for molecules exchange from and to the blood flow.

The device contains four electrodes, with a diameter of 600 µm and a geometrical surface area (GSA) of 0.0019 mm^2 (500-µm opening). Feedlines are 200-µm wide. The electrodes cover an area of ≈7.6 × 3.6 mm^2 (Figure 1c). The total length of the device is 44 mm, and its largest width is 7.6 mm. A V-shaped area at the tip is used to smoothen the insertion of the device into the catheter. The total thickness is ≈77 µm, limited by the high viscosity of the PCL-based solution and the depth of the engraved pattern necessary to deposit the PEDOT:PSS-based solution smoothly.

PCL has been recently considered in vascular applications, including grafts and stents. The former usually fabricated via electrospinning, and the latter by printing. Hemocompatibility is affected by the fabrication process since surface roughness strongly correlates to cell adhesion and platelet activation processes.[25] Smooth PCL, compared to electrospun mats, showed better interaction with blood.[26] Also, PCL-based stents fabricated via 3D printing demonstrated good hemocompatibility.[27] For this neurovascular interface, the fabrication via spin-coating resulted in a surface qualitatively similar to casted mats or 3D printed devices rather than electrospun mats (Figure 1d). However, laser cutting might introduce localized roughness at the edges. Hemocompatibility of polymeric stents made out by laser cutting have been already investigated, showing that, although activation of the coagulation cascade occurred, it was within a safe range of values.[28] Nevertheless, the hemocompatibility of this device remains to be evaluated in a future study.

2.2. Electrochemical Characterization in Static Condition

Impedance spectroscopy (**Figure 2**a) performed in phosphate buffered solution (PBS) after fabrication revealed a predominantly resistive behavior of the electrodes, given by the flatness of the magnitude plot (Figure 2a, black) and the phase angle approaching 0° (Figure 2a, blue) over a wide range of frequencies (10^1–10^5 Hz).[29] The average (± s.d.) cut-off frequency, corresponding to a phase angle of −45°, was 2.22 ± 1.11 Hz (n = 20 electrodes from N = 5 devices; Figure 4b) and relevant frequencies in neural recording (1–300 Hz for local field potentials and 300–3000 Hz for extracellular spikes) are above it.[30] At the reference frequency for neural spikes recording (1 kHz), the average (±s.d.) impedance magnitude was 5.50 ± 3.00 kΩ, and the average (±s.d.) impedance phase angle was −0.84 ± 0.55° (n = 20 electrodes from N = 5 devices; Figure 2c,d). Cyclic voltammetry (Figure 2e), performed at a scan rate of 50 mV s^{-1} from −0.9 to 0.8 V, indicated a prevalent double-layer

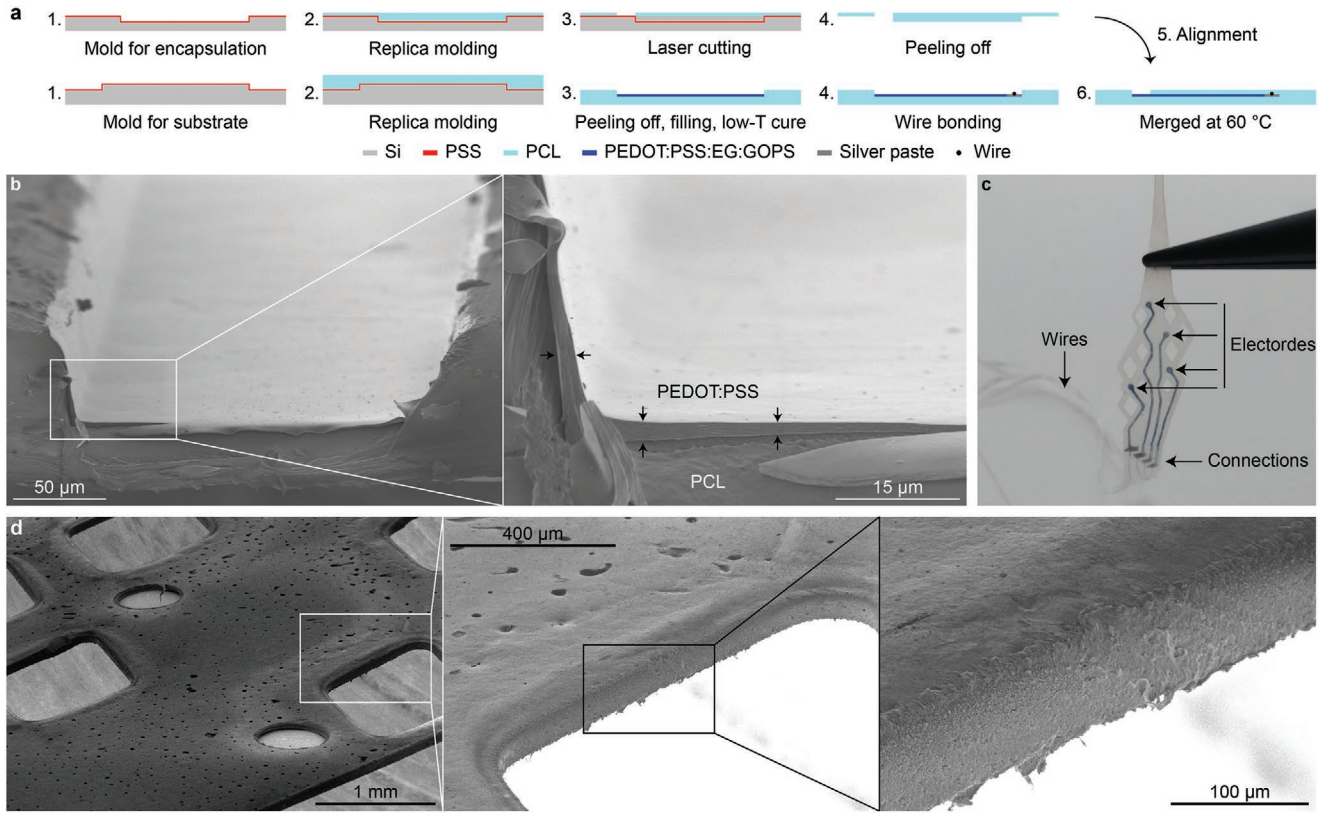

Figure 1. a) Sketch of the fabrication process. b) Scanning electron microscope image showing the cross-section of a feedline filled with the conductive polymer before encapsulation. The conductive polymer layer is indicated in the magnification by the black arrows. c) Picture of the transient neurovascular interface after fabrication. d) Scanning electron microscope images at different magnifications of the device side view after laser cut.

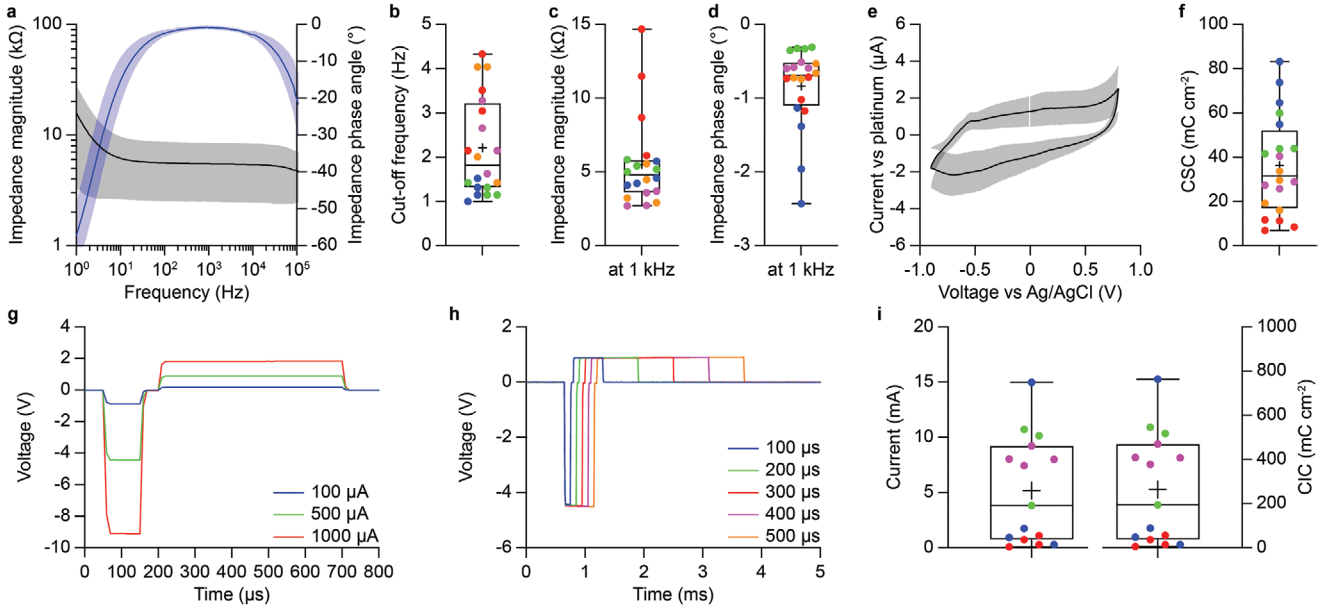

Figure 2. a) Average (±s.d.) impedance magnitude (black, left axis) and impedance phase angle (blue, right axis) plots. Solid lines are the averages ($n = 20$ electrodes from $N = 5$ devices) and shaded areas are the standard deviations. b) Quantification of the cut-off frequency, c) the impedance magnitude at 1 kHz and d) the impedance phase angle at 1 kHz. Different colors correspond to electrodes from different devices. e) Average (±s.d.) cyclic voltammetry plot. The solid line is the average ($n = 20$ electrodes from $N = 5$ devices) and the shaded area is the standard deviation. f) Quantification of the CSC. Different colors correspond to electrodes from different devices. g,h) Representative VTs at g) different current amplitudes and h) pulse widths. i) Box plots of the maximum injectable currents (left axis) and CIC (right axis). Different colors correspond to electrodes from different devices.

capacitance and its integral resulted in a mean total charge storage capacity (CSC) of 42.02 ± 26.89 mC cm^{-2} (n = 20 electrodes from N = 5 devices; Figure 2f).

It is to be noted that PBS and blood have similar conductivity (respectively 1.6 and 0.7 S m^{-1}) and viscosity (respectively 1 and 4 cP).[7,31–34] Nevertheless, impedance spectroscopy (Figure S1a, Supporting Information) and cyclic voltammetry (Figure S1e, Supporting Information) performed in PBS have been compared to measures performed in animal blood, to rule out any effect of the medium (n = 4 electrodes from N = 1 device). The cut-off frequency (p = 0. 0.125, Wilcoxon matched-pairs signed rank test; Figure S1b, Supporting Information), the impedance magnitude at 1 kHz (p = 0.125, Wilcoxon matched-pairs signed rank test; Figure S1c, Supporting Information), the impedance phase angle at 1 kHz (p = 0.125, Wilcoxon matched-pairs signed rank test; Figure S1d, Supporting Information) and the CSC (p = 0. 0.125, Wilcoxon matched-pairs signed rank test; Figure S1f, Supporting Information) were not statistically different. However, the cyclic voltammetry plot showed a high anodic peak above 0.5 V, which might be related to Fe^{2+} oxidation to Fe^{3+} or other interactions with biological molecules (i.e., ascorbic and uric acid, cysteine, or melatonin).[35,36]

To further characterize the device for neural stimulation, voltage transients (VTs) have been investigated, and the charge injection capacity (CIC) has been computed. Each electrode of 4 devices has been stimulated with low-current pulses repeated at 150 Hz until stabilization of the interface polarization was reached. Afterward, the CIC was tested: the injected current has been increased until the most negative (E_{mc}) or the most positive (E_{ma}) maximum polarization exceeded the water window of oxidation and reduction potentials (−0.9 or 0.8 V). All pulses were cathodic first, asymmetric (1:5 cathodic to anodic ratio), charge-balanced with a 50-µs interphase period. VTs showed a rectangular shape with a significant ohmic drop related to the mostly resistive behavior of the electrodes, visible as well from impedance spectroscopy. This VT waveform is maintained for different injected currents within the maximum limit (Figure 2g) and different pulse widths (Figure 2h). Also, the open circuit voltage of the electrode remained constant for stimulations with different pulse widths (from 100 to 500 µs, steps of 100 µs), suggesting no irreversibility in the charge injection.[29] The maximum injectable current has been tested with stimuli of 100-µs duration (cathodic phase). The average (± s.d.) maximum injectable current (always limited by the E_{mc}) was found to be 5.2 ± 4.8 mA (n = 15 electrodes from N = 4 devices) and the respective CIC was 263.6 ± 247.5 mC cm^{-2} (Figure 2i). Currents used in metallic stent-electrode arrays fall within the range sustainable by the polymeric electrode presented in this article.[6]

The electrochemical characterization showed the potential of the transient neurovascular interface for neural recording and stimulation. The low impedance over a wide frequency range is promising for favorable signal-to-noise ratio in recordings.[8] The high CSC (an index of the electrode charge transfer capabilities)[37] and CIC are promising for neurostimulation. It must be noted though that the CSC is usually an overestimation of the charge transfer potential of the electrodes: in fact when stimulating in vivo, at high frequencies and short pulses, only the superficial layers of the bulk PEDOT:PSS film will be active.[8] Thus, the CIC is expected to be lower than the CSC (typically CIC is 5–20% of the CSC for metals and oxides).[29] In our measurements, PEDOT:PSS electrodes reported a CIC higher than the total CSC with high variability among electrodes. A similar trend has been reported already in literature for PEDOT-coated PtIr electrodes.[38] A factor contributing to the high CIC is the positive open circuit potential reached by the electrodes after a prolonged stimulation at low current pulses to reach stabilization at the electrode-electrolyte interface. This open circuit potential was positive for all electrodes (≈0.25 V for most electrodes with a few exceptions at 0.15 V), leading most electrodes to a positive E_{mc} value for injected currents below 1500 µA.

Next, the device has been tested for prolonged charge injection by exposing the electrodes to 4 million pulses delivered at 200 Hz of repetition rate. The amplitude of the cathodic pulse was set to 500 µA and the duration to 100 µs (50 nC per phase). VTs have been measured at several timepoints during the stimulation protocol: at the start and after 50k, 100k, 200k, 500k, 750k, 1M, 2.5M, and 4M stimuli using the electrochemistry three-electrode setup (**Figure 3**a,b). The E_{mc} over pulses was quantified as a parameter for the electrode stability (Figure 3c). Out of the 12 electrodes tested from 3 devices, in 11 electrodes the E_{mc} remained within the water window limit (Figure 3c, dashed line), while 1 electrode exceeded this value after 100k pulses. For most electrodes (10 out of 12), the E_{mc} remained stable over the entire protocol of 4M pulses. Electrodes also showed no sign of damage after 4M pulses (Figure 3d).

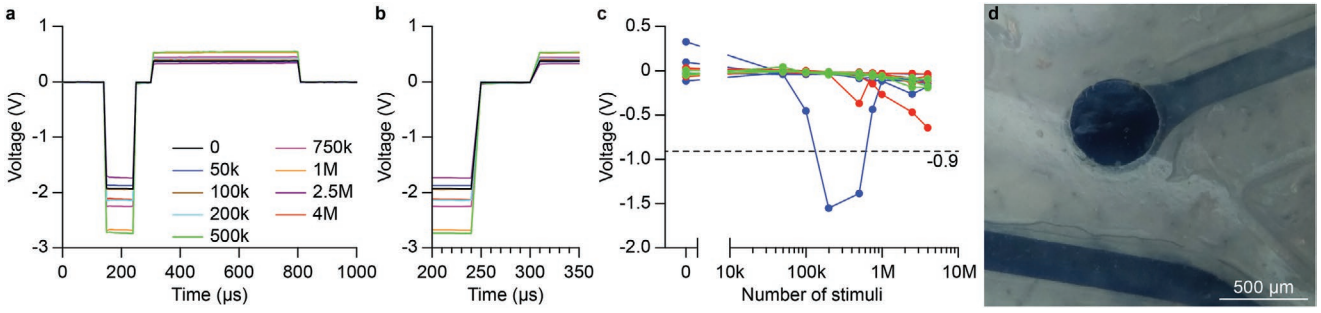

Figure 3. a) VTs during prolonged stimulation at several timepoints. Representative example from 1 electrode. b) Magnification of the VTs in (a) after the cathodic drop for the quantification of the E_{mc}. c) Quantification of the E_{mc} during prolonged stimulation (n = 12 electrodes from N = 3 devices). Each color highlights electrodes from the same device. d) Microscope image of a representative electrode after being exposed to 4M pulses.

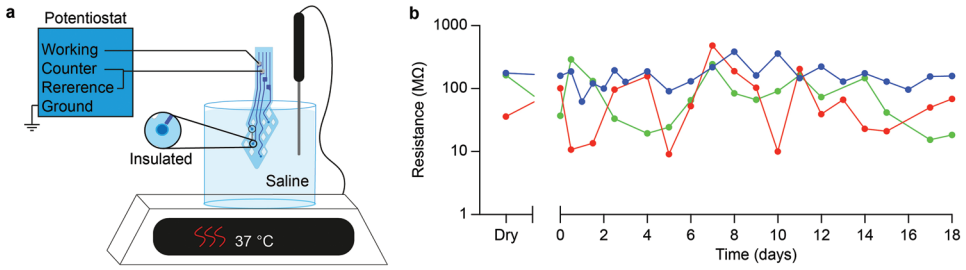

Figure 4. a) Sketch of the set-up for the measurement of the resistance between encapsulated electrodes. b) Quantification overtime of the resistance between pairs of electrodes ($n = 3$ pairs from $N = 3$ devices).

Last, we evaluated the insulation resistance in between feedlines to validate the absence of crosstalk between the electrodes. To unambiguously rule out electrode crosstalk, we fabricated fully encapsulated devices (i.e., without electrode openings)[39] and measured the resistance between 3 pairs of neighboring electrodes, one pair of electrodes per device (**Figure 4**a). Resistance measure has been performed in dry condition (i.e., after fabrication) and while the device was immersed in saline solution (0.9% NaCl) at 37 °C for up to 18 days (Figure 4b). All the measures showed that the electrical resistance remained very high (>10 MΩ) despite immersion in saline solution, and comparable to the values measured in dry condition. PCL is a slow degrading polymer. Therefore, the electrical insulation of the feedlines is expected to last for several weeks.

2.3. Delivery of the Device

We investigated the device compatibility with a standard stent delivery approach (**Figure 5**a). The shape of the device has been optimized for a smooth insertion inside the delivery catheter thanks to the V-shaped tip allowing for a gradual bending and adaptation of the device to the cylindrical catheter. The device could be attached to a push wire (0.36-mm diameter) and navigated inside a 5-Fr catheter (1.67-mm outer diameter). During navigation inside the catheter, the device is constrained by the catheter. When deployed, it will tend to restore its original planar configuration with minimal deformation (Figure 5c). This expansion promises good adherence when deployed inside a blood vessel. Also, the navigation inside the catheter and the deployment did not affect the mechanical integrity of the device (Figure 5b,c).

Impedance spectroscopy (Figure 5d) and cyclic voltammetry (Figure 5h) have been performed before and after deployment of the device using a 5-Fr catheter ($n = 4$ electrodes from $N = 1$ device). The cut-off frequency ($p = 0.625$, Wilcoxon matched-pairs signed rank test; Figure 5e), the impedance magnitude at 1 kHz ($p = 0.125$, Wilcoxon matched-pairs signed rank test; Figure 5f), the impedance phase angle at 1 kHz ($p = 0.125$, Wilcoxon matched-pairs signed rank test; Figure 5g) and the CSC ($p = 0.250$, Wilcoxon matched-pairs signed rank test; Figure 5i) were not statistically different before and after deployment.

2.4. Endurance of the Device in Dynamic Condition

Devices has been inserted in a 2-mm channel (made out of polydimethylsiloxane) filled with PBS at 37 °C and connected to a peristaltic pump, generating a pulsatile flow inside the channel, to investigate the electrochemical behavior over time in an environment modeling the vasculature (**Figure 6**a). The flow was set at ≈106 mL min^{-1} to simulate the cerebral venous flow of Yucatan pigs (108 mL min^{-1}), which is the envisioned animal model for further in vivo validation of the device.[40] Electrodes have been monitored for 30 days measuring impedance spectroscopy and cyclic voltammetry ($n = 12$ electrodes from $N = 3$ devices; respectively Figure 6b–d). The cut-off frequency could not be measured since the phase angle never reached −45° in the tested range of frequencies (Figure 6c). The change in the profile of the phase angle, and the overall higher magnitude plot is not caused by the release of the device from the catheter, but it can be explained by the changes in the geometry of the electrolytic cell, owed to the interposition of the channel volume between the device and the reference and counter electrodes which are left in the bath. Instead of the cut-off frequency, the impedance magnitude at 10 Hz (Figure 6e) and 1 kHz (Figure 6f) and the CSC (Figure 6g) normalized to their respective initial values (day 0) have been used as parameters to assess the electrode endurance. Overall, 10 out of 12 electrodes remained functional for 30 days, while 2 electrodes from one probe stopped functioning: 1 after 21 days and 1 after 30 days (blue empty circles in Figure 6e–g indicated by E on the y axis).

The impedance magnitude plot remained stable for 10 days (Figure 6b), and it started increasing from day 15. After 30 days, the impedance magnitude increased by 1.78 times and 1.74 times of its original value, respectively, at 10 Hz (Figure 6e) and 1 kHz (Figure 6f). The total CSC increased to 1.20 times of its original value (Figure 6g). The reason why the impedance module increased and, at the same time, the CSC increased as well is not yet clear. The increase in impedance over time might be attributed to two factors: a deterioration of the electrodes or a tightening of the device-wall interface. On the other hand, the increase of the CSC might be explained by the swelling of PEDOT:PSS.[41–43] Furthermore, this swelling would cause diffusion of electrolyte within the PEDOT:PSS network and its penetration into those areas covered by the encapsulation layer, increasing the effective GSA of the electrode. The electrolyte leakage is detectable at slow scanning rates (50 mV s^{-1}) but not at high scanning rates since the pore resistance represents an obstacle limiting the access to the area under the encapsulation.[29] Therefore, cyclic voltammetry would be affected by this phenomenon, while impedance measurements at 1 kHz and 10 Hz would not.

For a prolonged investigation, one device has been left inside the pulsatile system for additional 30 days: the impedance module at 10 Hz reached 1.96 times its original value

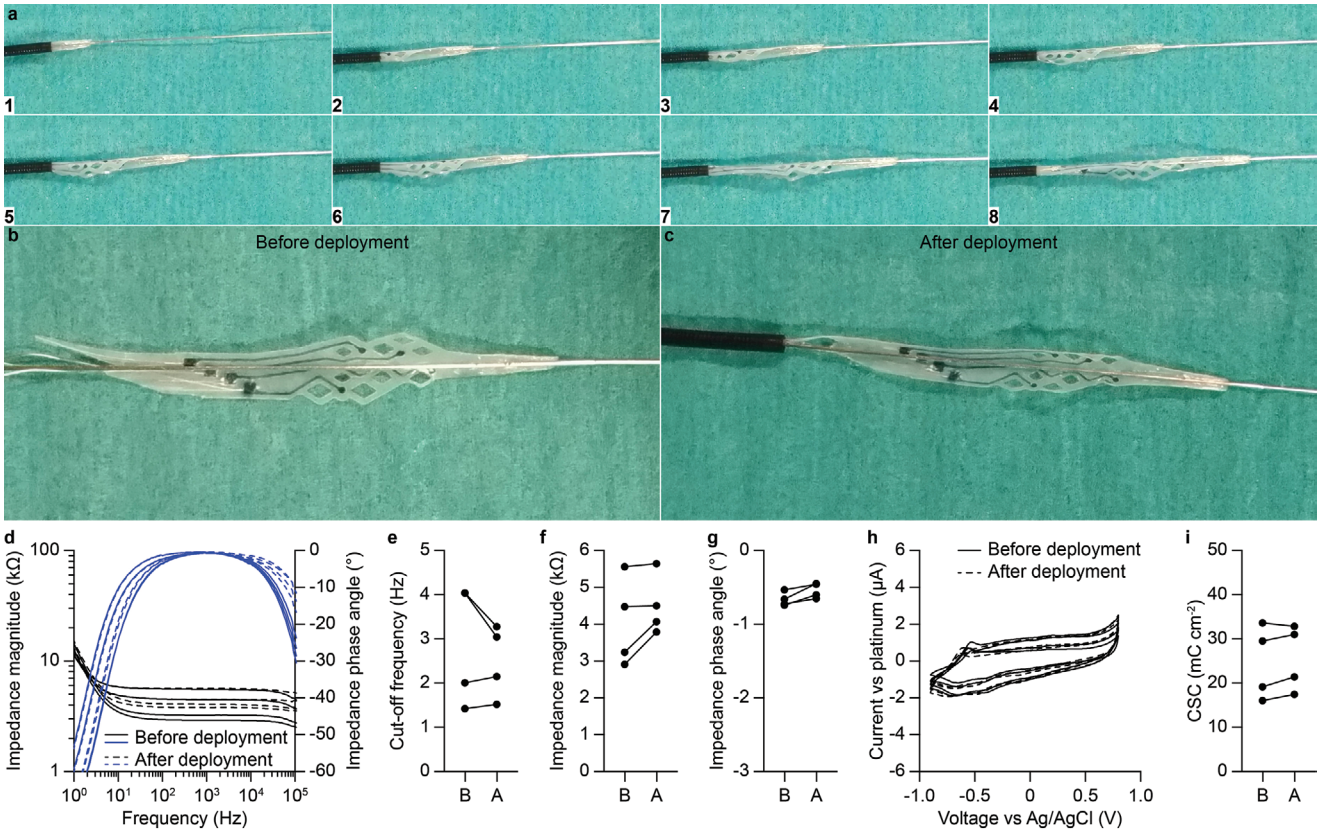

Figure 5. a) Image sequence of the deployment of the device using a 5-Fr catheter. b,c) Comparison of the device b) before and c) after navigation and deployment. d) Impedance magnitude (black, left axis) and impedance phase angle (blue, right axis) plots before (solid lines) and after (dashed lines) deployment of the device using a 5-Fr catheter ($n = 4$ electrodes from $N = 1$ device). e) Quantification of the cut-off frequency, f) the impedance magnitude at 1 kHz and g) the impedance phase angle at 1 kHz before (B) and after (A) deployment of the device using a 5-Fr catheter. h) Cyclic voltammetry plot before (solid lines) and after (dashed lines) deployment of the device using a 5-Fr catheter ($n = 4$ electrodes from $N = 1$ device). i) Quantification of the CSC before (B) and after (A) deployment of the device using a 5-Fr catheter.

($n = 4$, Figure 5h), the impedance module at 1 kHz reached 1.98 times its original value ($n = 4$, Figure 6i) and the CSC decreased to 0.86 times its original value ($n = 4$, Figure 6j) at day 60.

These results suggest that the device is still functional after two months, even if signs of electrodes damage appeared in some electrodes after two weeks.

2.5. Device Apposition to a Cylindrical Structure

The transient neurovascular interface is designed to expose polymeric electrodes around a cylindrical surface (e.g., facing a vessel wall). Therefore, we deployed the device inside a 2-mm diameter channel built in rigid poly(methyl methacrylate) (PMMA) to evaluate the device apposition once released (**Figure 7**a). Apposition has been measured using micro-computed tomography (micro-CT) scans. Once deployed in the channel, the device will naturally try to restore its original planar shape, thus adhering to the wall and remaining constrained in place. The micro-CT scan has been carried out at 10-μm resolution, and both the longitudinal (Figure 7b) and transversal (Figure 7c–e) cross-sections of the channel have been analyzed. The cross-sections showed a good device apposition against the channel with the lumen almost entirely maintained. Nevertheless, a few gaps between the device and the channel have been observed. On average (±s.d.), gaps were 98.1-μm long (± 42.4 μm, $n = 9$ for $N = 3$ cross-sections), sufficiently far from moderate gap values (180 μm) reported in the literature that could potentially affect the hemodynamics within the vessel.[44] The available lumen delimited by the device was on average (± s.d.) 2.57 mm^2 (±0.18 mm^2, $n = 9$ for $N = 3$ cross-sections). Compared to the original lumen of 3.14 mm^2, the deployment of the device caused a lumen reduction of 18%. In an ideal scenario of perfect apposition, the lumen reduction would be 15% (device thickness = 77 μm). Both values (18% and 15%) fall far from hemodynamically significant stenosis situations occurring at 50% lumen reduction.[45] It must also be noted that the release in a rigid PMMA block is a worst-case scenario. A more plausible behavior of the device in situ would be investigated using mock vessels, with mechanical properties closer to the vasculature that would favor a better apposition. Also, even though the device structure is stent inspired, its primary function is not the one of stents (opening a clogged vessel). Therefore, the expansion at the deployment must be sufficient enough to put the electrodes in contact with the vessel walls, but it will not expand the vessel structure as a stent would do.

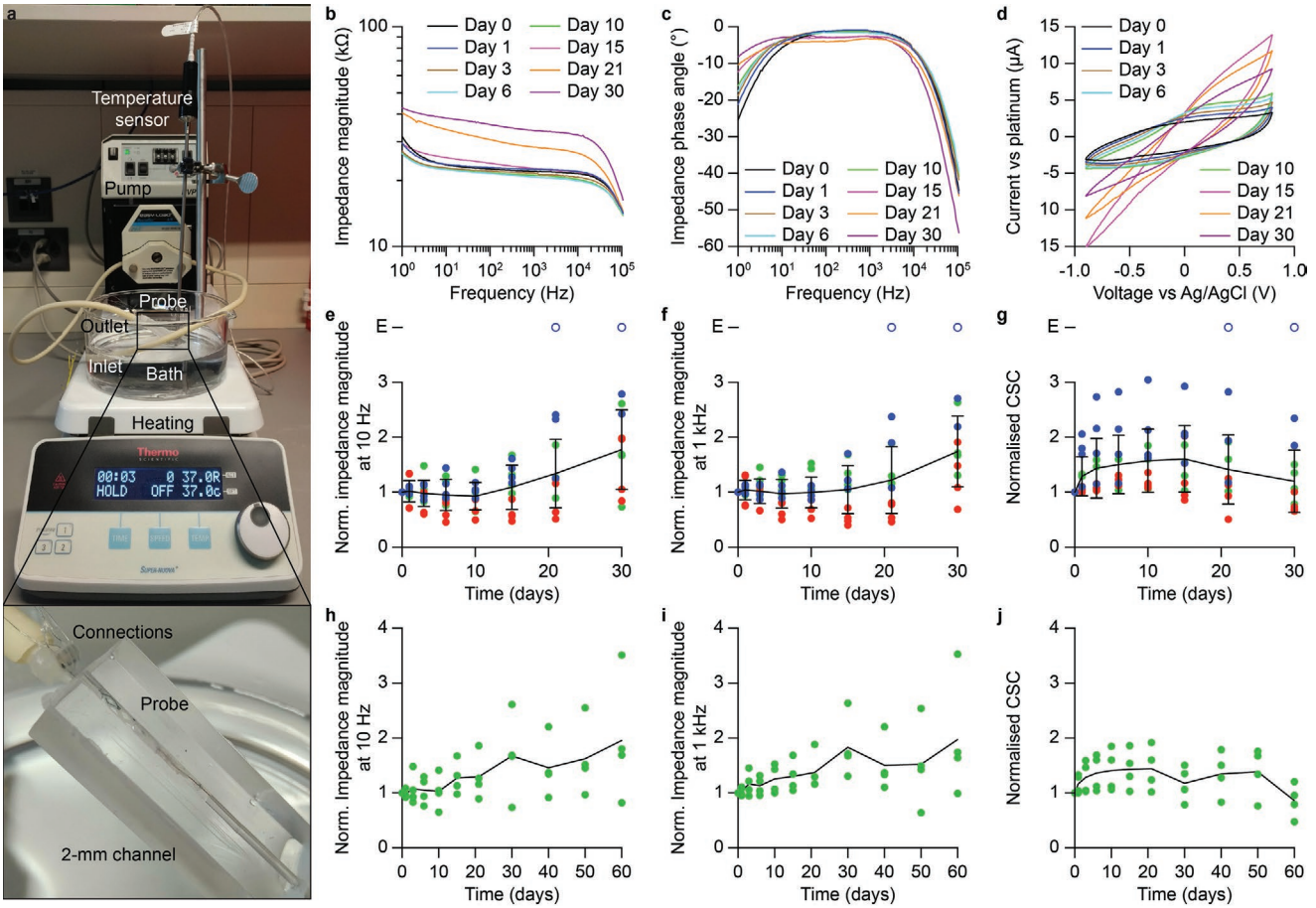

Figure 6. a) Picture of the experimental set-up showing: the hot-plate set at 37 °C, the temperature sensor, the beaker containing PBS and the tubes connected to the peristaltic pump and to the channel where the device is deployed. The magnification shows the device deployed in the 2-mm diameter channel. b) Average impedance magnitude, d) impedance phase angle, and d) cyclic voltammetry plots exposed for 30 days to pulsatile flow. e) Normalized impedance magnitude at 10 Hz, f) normalized impedance magnitude at 1 kHz and g) normalized CSC over 30 days. In each plot, different colors correspond to electrodes from different devices. The two empty circles show the two not functional electrodes. E means excluded. The solid line is the average with the standard deviation. h) Normalized impedance magnitude at 10 Hz, i) normalized impedance magnitude at 1 kHz, and j) normalized CSC over 60 days of one of the 3 devices (green). The solid line is the average.

2.6. Degradation Study

Last, we tested the degradation profile of the device. An advantage of synthetic degradable polymers is the possibility to tailor their degradation rate. When targeting the vasculature, it is crucial to match the degradation rate to the endothelialization and remodeling of the blood vessel and avoid chronic recoil and restenosis.[46] A slow degradation is an appealing feature for transient devices since it might allow for better tissue remodeling and reduced chronic trauma at the implantation site.[47–49,46] On the other hand, the PCL structure will likely last for several years before full degradation: a time that might largely exceeds the functionality of the PEDOT:PSS electrodes and what is needed to allow endothelialization and tissue remodeling. Therefore, we considered various blends of PCL and poly (D,L-lactic-co-glycolic acid) (PLGA) by mixing 85:15 PLGA (lactic acid: glycolic acid) with the PCL solution. Mixtures with different ratios of the two compounds have been prepared (80:20 and 70:30 PCL:PLGA) and devices have been fabricated and tested for accelerated in vitro degradation in PBS at 37 °C and pH 12 (**Figure 8**a,b). A fast degradation occurred for samples 80:20 and 70:30 since the beginning, while the pristine PCL started degrading around day 150. The composition 70:30 degraded to half its initial weight around the day 120. As expected, the degradation of the other mixtures is slower: the 80:20 composition degraded to half its initial weight around day 170 and pure PCL around day 260. The acceleration factor at pH 12 is estimated to be 2.5 for PCL (compared to degradation profiles at pH 7), therefore the composition 70:30 is expected to lose half its initial weight after ≈10 months.[47] It must be noted that accelerated ageing only evaluated the PCL degradation by hydrolysis, but PCL is also subjected to enzymatic degradation. Specifically, it has been reported that in vivo PCL undergoes a first degradation by hydrolysis lasting ≈12 months. Then, after its molecular weight is reduced to ≈3000, it is internalized by cells (macrophages, giant cells, and fibroblasts) and degraded by them.[20] Therefore, with accelerated tests, the degradation time might be overestimated.

According to ISO 10993–5: Biological Evaluation of Medical Devices, in vitro cytotoxicity has been evaluated via an extraction

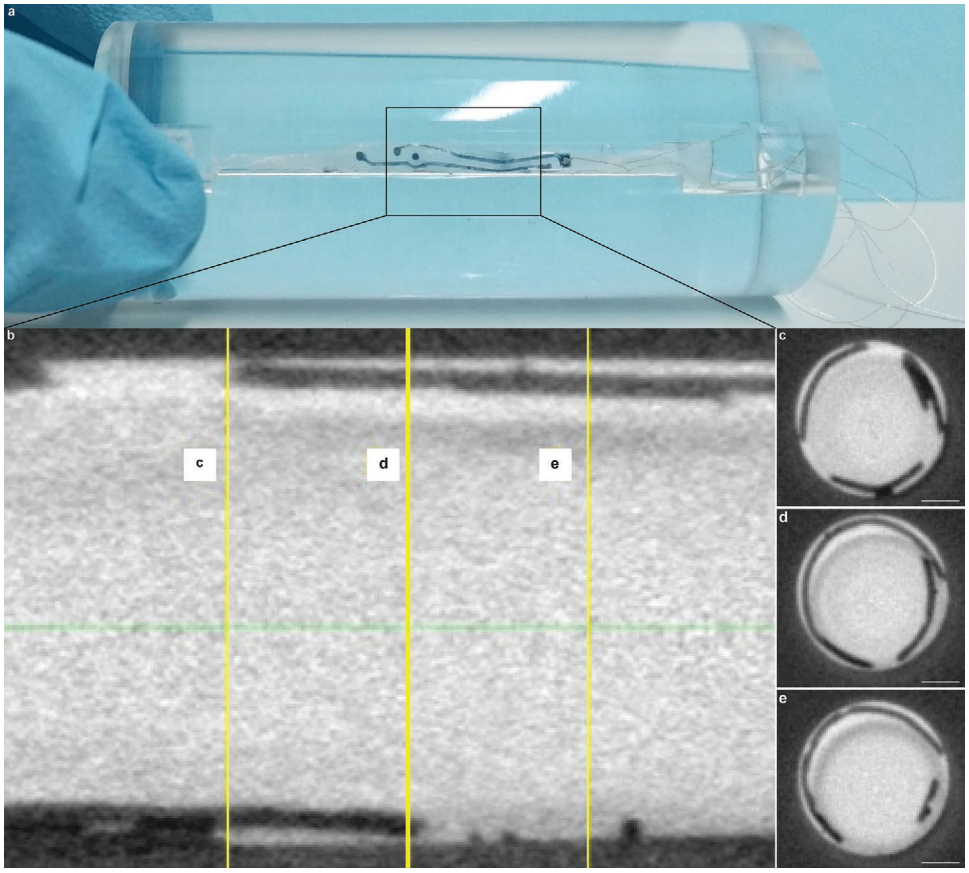

Figure 7. a) Picture of the transient neurovascular interface deployed inside a 2-mm sized channel made out of a PMMA. b) Micro-CT image showing the longitudinal cross-section of the device deployed inside the channel. In bright is the contrast agent injected inside the channel. c–e) Transversal cross-sections corresponding to the yellow c, d, e, positions in (b). The scale bars in panels (c–e) are 500 µm.

test on the murine fibroblastic L929 cells. Notably, in our test, the device did not show any sign of cytotoxicity (Figure 8c).

3. Conclusion

This work aimed at developing a minimally invasive transient neural interface to target the neural tissue from within a blood vessel.

The device has been successfully fabricated with a simple process employing standard cleanroom techniques, which allows for better encapsulation and reproducibility compared to handmade fabrication of metallic stents. Nonetheless, it must be noted that it involved a manual step for the deposition of the PEDOT:PSS-based conductive solution, which could affect the device reproducibility. The advantage of the current PEDOT:PSS deposition system inside grooves is the low amount of conductive polymer needed to fill one electrode unit (≈2 µL). This solution limits substantial waste of material, for example, such as during spin-coating.[50] Patterning PEDOT:PSS using lithography techniques either by lift-off or using a protective layer would be challenging since the compatibility of these processes with synthetic biodegradable polymers such as PCL is limited by its poor resistance to solvents or temperatures higher than 50 °C.[51] An exciting solution could be using a printing system to automatically move a microinjector along the pattern to deposit the conductive polymer homogeneously. Printing of PEDOT:PSS-based solutions is an open research topic, and a standard protocol is not yet defined. So far, mostly ink-jet printing has been used for patterning PEDOT:PSS on solar cells, low-cost in vitro electrophysiology systems and circuitry design on textiles.[50–54]

While PCL undergoes slow bulk degradation by hydrolysis and enzymatic reactions, the stability or degradability of pure PEDOT:PSS electrodes in the body is still elusive, regardless of its extensive usage as a coating of metal electrodes in neuroprosthetics.[21–23,55,56] Only a few studies have reported so far chronic performances of PEDOT:PSS in vivo.[57–60] Results showed performance drop after a few months of implantation. Given the high complexity of the biological environment, many different factors could contribute to the deterioration and degradation of PEDOT:PSS in vivo. A commonly reported failure mechanism is related to the adhesion of PEDOT:PSS to the substrate, such as metal electrodes.[61] Although bond strength and substrate adhesion can be enhanced using GOPS,[24] in the transient neurovascular interface, the weak adhesion between PEDOT:PSS and polyesters[62] is crucial since PEDOT:PSS might be subjected to water-induced swelling and delamination during the degradation of the PCL scaffold.[46] Moreover, PEDOT has been reported to be susceptible to hydrolysis when exposed to salt aqueous solutions[63] and it can be degraded

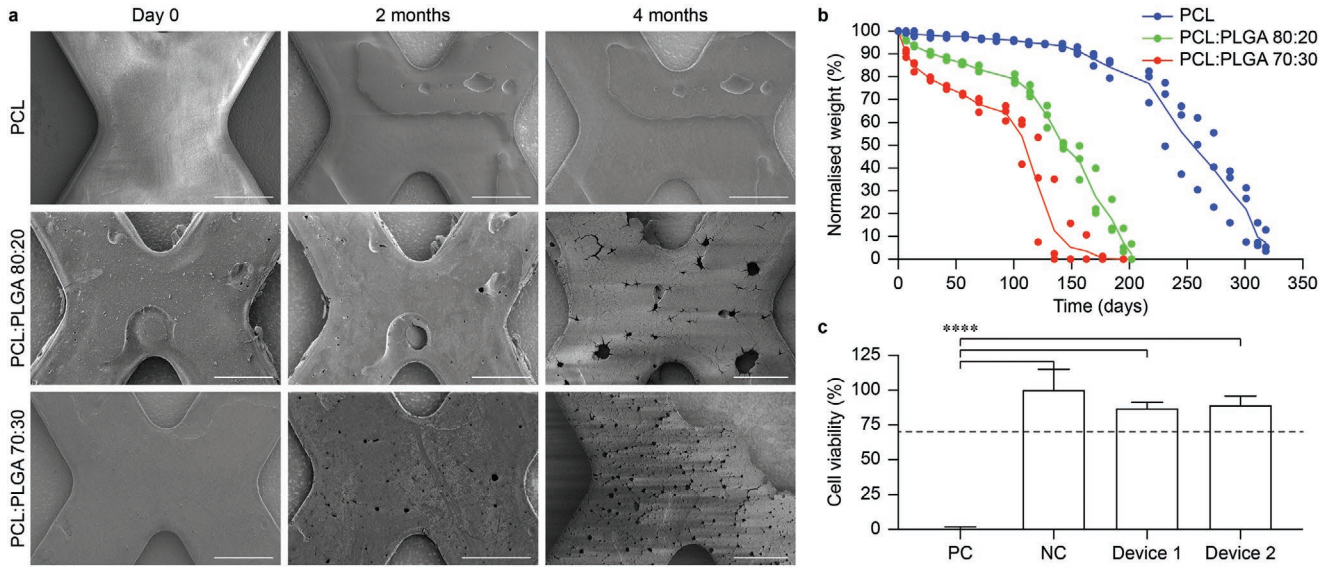

Figure 8. a) Scanning electron microscopy images of PCL, PCL:PLGA 80:20, and PCL:PLGA 70:30 samples during degradation. b) Normalized weight of PCL (blue), PCL:PLGA 80:20 (green) and PCL:PLGA 70:30 (red) samples during degradation. Solid lines are the averages. c) Quantification of in vitro cytotoxicity (mean ± s.d.) for each condition tested: positive control, 0 ± 1.81% (2 samples, 3 replicas per sample); negative control, 100 ± 15% (2 samples, 3 replicas per sample); transient neurovascular interface, 87 ± 4.14% and 89 ± 6.74% (2 devices, 3 replicas per device). One-way ANOVA: $F = 108.5$ and $p < 0.0001$. Tukey's multiple comparisons test: positive control versus negative control, $p < 0.0001$; positive control versus device 1, $p < 0.0001$; positive control versus device 2, $p < 0.0001$; negative control versus device 1, $p = 0.2891$; negative control versus device 2, $p = 0.4234$; device 1 versus device 2, $p = 0.9943$.

by high concentration of hydrogen peroxide, which is a physiological oxidant.[64,65] Another study reported that macrophages cultured with PEDOT:PSS generated a significant amount of hydrogen peroxide, that plays a critical role in the regulation of initiation and outcome of cellular phagocytosis.[66] Given the physiological presence of activated macrophages and hydrogen peroxide during inflammation and remodeling processes following device implantation, PEDOT:PSS could possibly be degraded by the combination of hydrolysis, hydrogen peroxide and macrophage uptake. In-depth studies about the fate of PEDOT-based polymers in vivo are required.

The device has been successfully navigated into a standard 5-Fr catheter and deployed inside a 2-mm diameter channel built in a rigid PMMA block. After deployment, the device induced a lumen reduction of only 18%, largely below the threshold to observe hemodynamically significant stenosis (50%). However, the validated delivery system uses a guidewire as a support for the device. The two are attached with glue to ensure effective navigation. Once the device is deployed, it would be ideal to detach the two elements. Possible strategies could involve using temporary glue that would dissolve after deployment or using coil embolization wires. The latter is a guidewire with a detachable coil at the end. The detachment is carried out by applying a current to the guidewire, leading to the rupture of the attachment point. Nevertheless, the Stentrode, built over a stent-retriever consisting of a nitinol stent attached to a metallic shaft, is currently being validated in a clinical trial with its shaft used as support for the wires and, thus, chronically implanted in the superior sagittal sinus through the transverse sinus without adverse effects so far.[3,5] Therefore, unless detachable solutions are found, in vivo validation of the device with the current delivery system could still be considered. Similarly, conductive wires are attached to the device. For the attachment we have used a general-purpose silver paste. However, electrically conductive epoxy pastes are undergoing ISO 10 993 validation with already good preliminary results.

Overall, these results set a good starting point for acute experimentation in vivo. Future work will also focus on the hemocompatibility of the device.

4. Experimental Section

Fabrication: Devices were fabricated using a molding technique. Two master molds were fabricated: one with protruding pattern of pads, feedlines, and electrodes (substrate mold) and the other one with engraved parts in correspondence of the feedlines (encapsulation mold). The molds were fabricated by SU8 GM1070 coating (1500 rpm, 35 µm) and patterning on 4-inch Si wafers, using standard photolithography (MLA150, Heidelberg Instruments). After hard baking of the molds, a release layer (PSS 18 wt% in H_2O; 561 223, Sigma Aldrich) was spin coated on both of them and baked at 145 °C for 10 min. Then, PCL (MW 50 000; 25 090, Polyscience, Inc.) was dissolved in chloroform (C2432, Sigma Aldrich) at 30% w/v and spin coated at 800 rpm on both molds. A soft bake for 30 min at 75 °C removed residual stresses caused by the spin-coating of the viscous solution. Solvent evaporation followed, leaving the wafers under a chemical hood at room temperature for 1 h. Electrode openings were laser cut (Optec MM200-USP) from the encapsulation layer and then both substrate and encapsulation layers were released by immersion in deionized water. The parameters of the laser cutter for the electrode openings were set as follow: speed 200 mm s^{-1}, jump speed 300 mm s^{-1}, laser firing rate 100 kHz/Hz, power 45%, laser ON-delay 85 µs, laser OFF-delay 135 µs, repetitions 40 and mode Galvo. The patterns on the substrate layer were filled with a solution of PEDOT:PSS (M122 PH1000, Ossila) mixed with 20 wt% EG (324 558,

Sigma Aldrich) and 1 wt% GOPS (440167, Sigma Aldrich), before curing overnight in an oven at 37 °C. After washing in deionized water to remove uncross-linked PEDOT:PSS monomers, Teflon coated stainless steel wires (114-µm diameter; Z-790500, Science Products GmbH) were connected to the pads using silver paste (G3692 Acheson Silver DAG 1415, PLANO GmbH). The encapsulation layer was then aligned to the substrate and attached to it by quickly melting the two layers at 60 °C. The outline of the complete device was then laser cut. The parameters of the laser cutter for the outline were set as follow: speed 300 mm s^{-1}, jump speed 300 mm s^{-1}, laser firing rate 100 kHz/Hz, power 35%, laser on delay 85 µs, laser off delay 135 µs, repetitions 30 and mode IFOV.

Electrochemistry: Electrochemical characterization was performed in a three-electrode configuration with a large area platinum counter electrode and a non-current carrying reference electrode (Ag/AgCl; BASMF2056, Sigma). The electrolytic cell was connected to a potentiostat (Compact Stat, Ivium) and electrochemical measurements were taken at room temperature with each device immersed in PBS at pH 7.2. Impedance spectroscopy was carried out between 1 and 10^5 Hz using a 50-mV AC voltage. Cyclic voltammetry curves were obtained by sweeping a cyclic potential at 50 mV s^{-1} scan rate between −0.9 and 0.8 V. For each electrode, the average response over 5 cycles was calculated and the total CSC was computed as the area within the curves. For tests performed in animal blood, blood samples were collected from euthanized C567BL6 mice using a 2-mL syringe and a 23-gauge needle, both pre-coated with Ethylenediaminetetraacetic acid 0.5 M at pH 8 (EDTA; E9884, Sigma). Samples were then transferred into a 2-mL Eppendorf tube containing 9 mg of EDTA per mL of blood. Blood was kept on a shaker at room temperature until use. The experiment was approved by the Département de l'emploi, des affaires sociales et de la santé, Direction générale de la santé of the Republique et Canton de Geneve in Switzerland (authorization GE/70/20).

Electrochemistry under Pulsatile Flow: A 2-mm diameter channel was fabricated with polydimethylsiloxane (Sylgard 184, Dow Corning) by molding. The device was inserted in the channel and connected to the tube (Nr.16 MasterFlex L/S PharMed) encased in the rotatory head (7518-10, Masterflex L/S Easy-Load) of a peristaltic pump (Ismatec). The tube and the channel were immersed in PBS (pH 7.2) inside a wide glass beaker placed onto a hotplate (Super-Nuova+, Thermo Scientific) whose temperature probe inside the PBS was set to 37 °C. The pump was set at 500 rpm. Electrochemical measurements of impedance spectroscopy and cyclic voltammetry were performed over time with the device inside the channel, using the beaker as electrolytic cell with a large area platinum counter electrode and a non-current carrying reference electrode (Ag/AgCl; BASMF2056, Sigma) immersed during measurements.

Voltage Transients: VTs were performed in the same three-electrode configuration used for electrochemistry, at room temperature with each device immersed in PBS at pH 7.2. The current pulses were asymmetric (1:5 cathodic to anodic ratio), charge-balanced, cathodic first with a 500-µs interphase period. First, electrodes were stabilized with low current pulses (100 or 10 µA, depending on the electrode capacity) at 150 Hz. Stabilization occurred within 6000 pulses and was followed by stimulations at increasing current amplitudes until the E_{mc} or the E_{ma} of the electrode exceeded the water window (–0.9–0.8 V). The E_{mc} and E_{ma} were defined as the voltage value measured after 10 µs from the end of the cathodic or anodic pulse to avoid the ohmic drop. 10 pulses were delivered for each current amplitude and the E_{mc} and E_{ma} values were the average of the repetitions. The maximum injectable current was defined as the maximum current with which the electrodes could be stimulated without their response exceeding the water window limit. The CIC was calculated by multiplying the maximum injectable current by the pulse width (cathodic phase) and dividing the obtained charge by the electrode GSA.

Resistance Measures: To measure the resistance, devices were immersed in saline solution (0.9% NaCl) at 37 °C and pH 7.2, and electrode pairs were connected to the potentiostat (Compact Stat, Ivium) and a voltage of 0.5 V was applied to measure the current generated. Resistance values were obtained by dividing the applied voltage by the measured current.

Long-Term Stimulation: Devices were immersed in saline solution (0.9% NaCl) at room temperature and pH 7.2. Up to 4 M current pulses were delivered using an isolated stimulus generator (STG4002, Multi Channel Systems) at 200 Hz of repetition rate. During stimulation, and a platinum wire was immersed in the bath as ground electrode. Current pulses were asymmetric (1:5 cathodic to anodic ratio), charge-balanced, cathodic first with a cathodic amplitude of 500 µA, a duration of 100 µs and a 60-µs interphase period. At several timepoints, a measure of VT was performed as described above using the potentiostat (Compact Stat, Ivium) in a three-electrode configuration and applying the same current pulse. The E_{mc} was defined as the voltage value measured after 30 µs from the end of the cathodic pulse to avoid the ohmic drop. For each timepoint, 8 current pulses were delivered and the final E_{mc} value was the average of the repetitions.

Degradation: PCL and PLGA (Resomer RG 858 S; 739979-5G, Sigma) were mixed at various ratios: 100:0, 80:20, and 70:30. The powder mix was dissolved in chloroform (C2432, Sigma-Aldrich) at 45 °C and with magnetic stirring at 200 rpm for 2 h. For each composition, 3 samples were prepared. The weight of the samples was recorded after fabrication and kept as a reference. Samples were immersed in 10-mL PBS at pH 12 at 37 °C. At each time point samples were taken out of the solution and dried at room temperature under vacuum for 4 h. Once dry, samples were weighted and, depending on the time point, scanning electron microscopy images were taken.

Delivery System: The top extremity of device was attached to the end of a push wire (STABILIZER 527-300E, 0.36 mm diameter, Cordis) using super glue (Supergel, UHU). The push wire with the device attached was then immersed in deionized water, and the target catheter (5Fr, NavienTM A+ 058, Intracranial Support Catheter, OD 1.7 mm) was filled with deionized water. This wetting is used to improve insertion and navigation of the device inside the catheter. The device attached to the push wire was then pushed inside the catheter and navigated until exiting after ≈1-m of navigation.

Microtomography Imaging: A channel was created in PMMA with a 2-mm diameter. The device was deployed inside the channel. To avoid metallic artifacts generated by the push wire, the attachment site was cut after deployment. To improve the device visibility within the channel, the channel was filled with a contrast agent (Iopamiro 300 mg mL^{-1}, Bracco) mixed with NaCl solution at 30% v/v. Imaging was performed at 10-µm resolution with a 5-mm field of view (Qunatum CT Lab GX, Rigaku microCT Technology and Perkin Elmer software).

Scanning Electron Microscopy: Images were taken with a Schottky field emission scanning electron microscope (SU5000, Hitachi) at 1 kV access voltage and 10% of maximum spot intensity.

Cytotoxicity Test: A test on extract was performed with devices sterilized by UV exposure, with a ratio of the product to extraction vehicle of 3 cm^2 mL^{-1}. The extraction vehicle was Eagle's minimum essential medium (11090081, Thermo Fisher Scientific) supplemented with 10% fetal bovine serum (10270106, Thermo Fisher Scientific), 1% penicillin-streptomycin (15070063, Thermo Fisher Scientific), 2 mM L-Glutamine (25030081, Thermo Fisher Scientific), and 2.50 µg mL^{-1} Amphotericin B (15290026, Gibco-Thermo Fisher Scientific). The extraction was performed for 24 h at 37 °C and 5% CO_2. L929 cells (88102702, Sigma) were plated in a 96 well plate at a sub-confluent density of 7000 cells per well in 100 µL of the same medium. L929 cells were incubated for 24 h at 37 °C and 5% CO_2. After incubation, the medium was removed from the cells and replaced with the extract (100 µL per well). After another incubation of 24 h, 50 µL per well of XTT reagent (Cell proliferation kit 11465015001, Sigma) were added and incubated for 4 h at 37 °C and 5% CO_2. An aliquot of 100 µL was then transferred from each well into the corresponding wells of a new plate, and the optical density was measured at 450 nm by using a plate reader (FlexStation3, MolecularDevices). Clean medium alone was used as a negative control, whereas medium supplemented with 15% of dimethyl sulfoxide (D2650-5×5ML, Sigma) was used as a positive control. Each condition was tested in triplicates.

Statistical Analysis and Graphical Representation: Statistical analysis and graphical representation were performed with Prism (Graph Pad). Normality test was performed in each dataset to justify the use of a parametric or non-parametric test. The box plots always extend from the

25th to 75th percentiles. The line in the middle of the box is plotted at the median. The + is the mean. The whiskers go down to the smallest value and up to the largest. In each figure *p*-values were represented as: * $p < 0.05$, ** $p < 0.01$, *** $p < 0.001$, and **** $p < 0.0001$.

Supporting Information

Supporting Information is available from the Wiley Online Library or from the author.

Acknowledgements

This work was supported by École polytechnique fédérale de Lausanne and Medtronic.

Conflict of Interest

The authors declare no conflict of interest.

Data Availability Statement

The data that support the findings of this study are available from the corresponding author upon reasonable request.

Keywords

endovascular device, neural interfaces, polymers, transient neurotechnology

Received: February 13, 2021
Revised: May 8, 2021
Published online:

[1] D. Borton, S. Micera, J. R. del Millán, G. Courtine, *Sci. Transl. Med.* **2013**, *5*, 210rv2.
[2] J. Z. Fan, V. Lopez-Rivera, S. A. Sheth, *Front. Neurosci.* **2020**, *14*, 432.
[3] T. J. Oxley, N. L. Opie, S. E. John, G. S. Rind, S. M. Ronayne, T. L. Wheeler, J. W. Judy, A. J. McDonald, A. Dornom, T. J. Lovell, C. Steward, D. J. Garrett, B. A. Moffat, E. H. Lui, N. Yassi, B. C. Campbell, Y. T. Wong, K. E. Fox, E. S. Nurse, I. E. Bennett, S. H. Bauquier, K. A. Liyanage, N. R. van der Nagel, P. Perucca, A. Ahnood, K. P. Gill, B. Yan, L. Churilov, C. R. French, P. M. Desmond, M. K. Horne, L. Kiers, S. Prawer, S. M. Davis, A. N. Burkitt, P. J. Mitchell, D. B. Grayden, C. N. May, T. J. O'Brien, *Nat. Biotechnol.* **2016**, *34*, 320.
[4] S. E. John, N. L. Opie, Y. T. Wong, G. S. Rind, S. M. Ronayne, G. Gerboni, S. H. Bauquier, T. J. O'Brien, C. N. May, D. B. Grayden, T. J. Oxley, *Sci. Rep.* **2018**, *8*, 8427.
[5] T. J. Oxley, P. E. Yoo, G. S. Rind, S. M. Ronayne, C. M. S. Lee, C. Bird, V. Hampshire, R. P. Sharma, A. Morokoff, D. L. Williams, C. MacIsaac, M. E. Howard, L. Irving, I. Vrljic, C. Williams, S. E. John, F. Weissenborn, M. Dazenko, A. H. Balabanski, D. Friedenberg, A. N. Burkitt, Y. T. Wong, K. J. Drummond, P. Desmond, D. Weber, T. Denison, L. R. Hochberg, S. Mathers, T. J. O'Brien, C. N. May, J. Mocco, D. B. Grayden, B. C. V. Campbell, P. Mitchell, N. L. Opie, *J. Neurointerv. Surg.* **2021**, *13*, 102.
[6] N. L. Opie, S. E. John, G. S. Rind, S. M. Ronayne, Y. T. Wong, G. Gerboni, P. E. Yoo, T. J. H. Lovell, T. C. M. Scordas, S. L. Wilson, A. Dornom, T. Vale, T. J. O'Brien, D. B. Grayden, C. N. May, T. J. Oxley, *Nat. Biomed. Eng.* **2018**, *2*, 907.
[7] B. A. Teplitzky, A. T. Connolly, J. A. Bajwa, M. D. Johnson, *J. Neural Eng.* **2014**, *11*, 026011.
[8] C. Boehler, S. Carli, L. Fadiga, T. Stieglitz, M. Asplund, *Nat. Protoc.* **2020**, *15*, 3557.
[9] T. D. Y. Kozai, A. S. Jaquins-Gerstl, A. L. Vazquez, A. C. Michael, X. T. Cui, *ACS Chem. Neurosci.* **2015**, *6*, 48.
[10] V. S. Polikov, P. A. Tresco, W. M. Reichert, *J. Neurosci. Methods* **2005**, *148*, 1.
[11] D. Prodanov, J. Delbeke, *Front. Neurosci.* **2016**, *10*, 11.
[12] S. McMahon, N. Bertollo, E. D. O. Cearbhaill, J. Salber, L. Pierucci, P. Duffy, T. Dürig, V. Bi, W. Wang, *Prog. Polym. Sci.* **2018**, *83*, 79.
[13] M. Gulino, D. Kim, S. Pané, S. D. Santos, A. P. Pêgo, *Front. Neurosci.* **2019**, *13*, 689.
[14] R. Biran, D. C. Martin, P. A. Tresco, *Exp. Neurol.* **2005**, *195*, 115.
[15] T. Saxena, L. Karumbaiah, E. A. Gaupp, R. Patkar, K. Patil, M. Betancur, G. B. Stanley, R. V. Bellamkonda, *Biomaterials* **2013**, *34*, 4703.
[16] R. Biran, D. C. Martin, P. A. Tresco, *J. Biomed. Mater. Res., Part A* **2007**, *82*, 169.
[17] S.-W. W. Hwang, H. Tao, D.-H. H. Kim, H. Cheng, J.-K. K. Song, E. Rill, M. A. Brenckle, B. Panilaitis, S. M. Won, Y.-S. S. Kim, Y. M. Song, K. J. Yu, A. Ameen, R. Li, Y. Su, M. Yang, D. L. Kaplan, M. R. Zakin, M. J. Slepian, Y. Huang, F. G. Omenetto, J. A. Rogers, *Science* **2012**, *337*, 1640.
[18] S.-K. Kang, R. K. Murphy, S.-W. Hwang, S. Lee, D. V. Harburg, N. A. Krueger, J. Shin, P. Gamble, H. Cheng, S. Yu, Z. Liu, J. G. McCall, M. Stephen, H. Ying, J. Kim, G. Park, C. R. Webb, C. Lee, S. Chung, D. Wie, A. D. Gujar, B. Vemulapalli, A. H. Kim, K.-M. Lee, J. Cheng, Y. Huang, S. Lee, P. V. Braun, W. Z. Ray, J. A. Rogers, *Nature* **2016**, *530*, 71.
[19] R. Li, L. Wang, D. Kong, L. Yin, *Bioact. Mater.* **2018**, *3*, 322.
[20] M. A. Woodruff, D. W. Hutmacher, *Prog. Polym. Sci.* **2010**, *35*, 1217.
[21] C. Bodart, N. Rossetti, J. Hagler, P. Chevreau, D. Chhin, F. Soavi, S. B. Schougaard, F. Amzica, F. Cicoira, *ACS Appl. Mater. Interfaces* **2019**, *11*, 17226.
[22] A. Schander, T. Tesmann, S. Strokov, H. Stemmann, A. K. Kreiter, W. Lang, *Annu. Int. Conf. IEEE Eng. Med. Biol. Soc.* **2016**, *2016*, 6174.
[23] D. Khodagholy, T. Doublet, M. Gurfinkel, P. Quilichini, E. Ismailova, P. Leleux, T. Herve, S. Sanaur, C. Bernard, G. G. Malliaras, *Adv. Mater.* **2011**, *23*, H268.
[24] A. Håkansson, S. Han, S. Wang, J. Lu, S. Braun, M. Fahlman, M. Berggren, X. Crispin, S. Fabiano, *J. Polym. Sci., Part B: Polym. Phys.* **2017**, *55*, 814.
[25] D. N. Sarode, S. Roy, *Expert Rev. Med. Devices* **2019**, *16*, 603.
[26] X. Dong, X. Yuan, L. Wang, J. Liu, A. C. Midgley, Z. Wang, K. Wang, J. Liu, M. Zhu, D. Kong, *Biomaterials* **2018**, *181*, 1.
[27] T. Qiu, W. Jiang, P. Yan, L. Jiao, X. Wang, *Front. Bioeng. Biotechnol.* **2020**, *8*, 462.
[28] M. Szymonowicz, Z. Rybak, W. Witkiewicz, C. Pezowicz, J. Filipiak, *Acta Bioeng. Biomech.* **2014**, *16*, 131.
[29] S. F. Cogan, *Annu. Rev. Biomed. Eng.* **2008**, *10*, 275.
[30] Z. Aqrawe, J. Montgomery, J. Travas-Sejdic, D. Svirskis, *Sens. Actuators, B* **2018**, *257*, 753.
[31] E. E. Tzirtzilakis, *Phys. Fluids* **2005**, *17*, 077103.
[32] P. H. Brown, A. Balbo, H. Zhao, C. Ebel, P. Schuck, *PLoS One* **2011**, *6*, e26221.
[33] S. Abdalla, S. S. Al-ameer, S. H. Al-Magaishi, *Biomicrofluidics* **2010**, *4*, 034101.
[34] P. Connes, T. Alexy, J. Detterich, M. Romana, M.-D. Hardy-Dessources, S. K. Ballas, *Blood Rev.* **2016**, *30*, 111.
[35] S. Chevion, M. Chevion, *Ann. N. Y. Acad. Sci.* **2006**, *899*, 308.
[36] H.-W. Wang, C. Bringans, A. J. R. Hickey, J. A. Windsor, P. A. Kilmartin, A. R. J. Phillips, *Signals* **2021**, *2*, 138.
[37] G. Schiavone, X. Kang, F. Fallegger, J. Gandar, G. Courtine, S. P. Lacour, *Neuron* **2020**, *108*, 238.

[38] S. Venkatraman, J. Hendricks, Z. A. King, A. J. Sereno, S. Richardson-Burns, D. Martin, J. M. Carmena, *IEEE Trans. Neural Syst. Rehabil. Eng.* **2011**, *19*, 307.
[39] M. F. Porto Cruz, M. Vomero, E. Zucchini, E. Delfino, M. Asplund, T. Stieglit, L. Fadiga, in *2019 9th Int. IEEE/EMBS Conf. on Neural Engineering (NER)*, IEEE, San Francisco, CA, USA, **2019**, pp. 924–927.
[40] C. A. Habib, D. Utriainen, J. Peduzzi-Nelson, E. Dawe, J. Mattei, Z. Latif, K. Casey, E. M. Haacke, *J. Magn. Reson. Imaging* **2013**, *38*, 641.
[41] B. Lu, H. Yuk, S. Lin, N. Jian, K. Qu, J. Xu, X. Zhao, *Nat. Commun.* **2019**, *10*, 1043.
[42] L. Bießmann, L. P. Kreuzer, T. Widmann, N. Hohn, J.-F. Moulin, P. Müller-Buschbaum, *ACS Appl. Mater. Interfaces* **2018**, *10*, 9865.
[43] M. Modarresi, A. Mehandzhiyski, M. Fahlman, K. Tybrandt, I. Zozoulenko, *Macromolecules* **2020**, *53*, 6267.
[44] W. X. Chen, E. K. W. Poon, V. Thondapu, N. Hutchins, P. Barlis, A. Ooi, *J. Biomech.* **2017**, *63*, 164.
[45] M. Thiriet, M. Delfour, A. Garon, in *PanVascular Medicine* (Ed: P. Lanzer), Springer, Berlin, **2015**, pp. 781–868.
[46] L. Ferlauto, P. Vagni, A. Fanelli, E. G. Zollinger, K. Monsorno, R. C. Paolicelli, D. Ghezzi, *Biomaterials* **2021**, *274*, 120889.
[47] U. Sharma, D. Concagh, L. Core, Y. Kuang, C. You, Q. Pham, G. Zugates, R. Busold, S. Webber, J. Merlo, R. Langer, G. M. Whitesides, M. Palasis, *Nat. Mater.* **2017**, *17*, 96.
[48] J. Shin, Y. Yan, W. Bai, Y. Xue, P. Gamble, L. Tian, I. Kandela, C. R. Haney, W. Spees, Y. Lee, M. Choi, J. Ko, H. Ryu, J.-K. Chang, M. Pezhouh, S.-K. Kang, S. M. Won, K. J. Yu, J. Zhao, Y. K. Lee, M. R. MacEwan, S.-K. Song, Y. Huang, W. Z. Ray, J. A. Rogers, *Nat. Biomed. Eng.* **2019**, *3*, 37.
[49] Y. Su, I. Cockerill, Y. Wang, Y.-X. Qin, L. Chang, Y. Zheng, D. Zhu, *Trends Biotechnol.* **2019**, *37*, 428.
[50] M. Y. Teo, N. RaviChandran, N. Kim, S. Kee, L. Stuart, K. C. Aw, J. Stringer, *ACS Appl. Mater. Interfaces* **2019**, *11*, 37069.
[51] B. Charlot, G. Sassine, A. Garraud, B. Sorli, A. Giani, P. Combette, *Microsyst. Technol.* **2013**, *19*, 895.
[52] S. H. Eom, S. Senthilarasu, P. Uthirakumar, S. C. Yoon, J. Lim, C. Lee, H. S. Lim, J. Lee, S.-H. Lee, *Org. Electron.* **2009**, *10*, 536.
[53] L. D. Garma, L. M. Ferrari, P. Scognamiglio, F. Greco, F. Santoro, *Lab Chip* **2019**, *19*, 3776.
[54] Y. Guo, M. T. Otley, M. Li, X. Zhang, S. K. Sinha, G. M. Treich, G. A. Sotzing, *ACS Appl. Mater. Interfaces* **2016**, *8*, 26998.
[55] T. Someya, Z. Bao, G. G. Malliaras, *Nature* **2016**, *540*, 379.
[56] D. Khodagholy, J. N. Gelinas, T. Thesen, W. Doyle, O. Devinsky, G. G. Malliaras, G. Buzsáki, *Nat. Neurosci.* **2015**, *18*, 310.
[57] A. Schander, H. Stemmann, E. Tolstosheeva, R. Roese, V. Biefeld, L. Kempen, A. K. Kreiter, W. Lang, *Sens. Actuators, A* **2016**, *247*, 125.
[58] H. Charkhkar, G. L. Knaack, D. G. McHail, H. S. Mandal, N. Peixoto, J. F. Rubinson, T. C. Dumas, J. J. Pancrazio, *Acta Biomater.* **2016**, *32*, 57.
[59] K. A. Ludwig, J. D. Uram, J. Yang, D. C. Martin, D. R. Kipke, *J. Neural Eng.* **2006**, *3*, 59.
[60] A. Schander, S. Strokov, H. Stemmann, T. Tebmann, A. K. Kreiter, W. Lang, *IEEE Sens. J.* **2019**, *19*, 820.
[61] G. Dijk, A. L. Rutz, G. G. Malliaras, *Adv. Mater. Technol.* **2020**, *5*, 1900662.
[62] F. Gong, C. Meng, J. He, X. Dong, *Prog. Org. Coat.* **2018**, *121*, 89.
[63] V. Sethumadhavan, K. Zuber, C. Bassell, P. R. Teasdale, D. Evans, *Commun. Chem.* **2020**, *3*, 153.
[64] E. M. Thaning, M. L. M. Asplund, T. A. Nyberg, O. W. Inganäs, H. von Holst, *J. Biomed. Mater. Res.* **2010**, *93B*, 407.
[65] T. Chen, Y. Lin, X. Bi, Y. Gu, *Mater. Chem. Phys.* **2020**, *242*, 122509.
[66] H. Gong, J. Xiang, L. Xu, X. Song, Z. Dong, R. Peng, Z. Liu, *Nanoscale* **2015**, *7*, 19282.